Electronic band structure of Ti$_2$O$_3$ thin films studied by angle-resolved photoemission spectroscopy

Naoto Hasegawa,[1] Kohei Yoshimatsu ⓘ,[1,2,*] Daisuke Shiga ⓘ,[1] Tatsuhiko Kanda ⓘ,[1] Satoru Miyazaki,[1] Miho Kitamura,[3]
Koji Horiba,[3] and Hiroshi Kumigashira ⓘ[1,2,3]

[1]*Institute of Multidisciplinary Research for Advanced Materials (IMRAM), Tohoku University, Sendai 980-8577, Japan*
[2]*Materials Research Center for Element Strategy (MCES), Tokyo Institute of Technology, Yokohama 226-8503, Japan*
[3]*Photon Factory, Institute of Materials Structure Science, High Energy Accelerator Research Organization (KEK), Tsukuba 305-0801, Japan*

Ti$_2$O$_3$ exhibits a unique metal-insulator transition (MIT) at ∼450 K over a wide temperature range of ∼150 K. This broad MIT accompanied by lattice deformation differs from the sharp MITs observed in most other transition-metal oxides. A longstanding issue is determining the role of electron-electron correlation in the electronic structure and MIT of Ti$_2$O$_3$. However, the lack of information about the band structure of Ti$_2$O$_3$ has hindered investigating the origin of its unusual physical properties. Here, we report the electronic band structure of "insulating" Ti$_2$O$_3$ films with slight hole doping by angle-resolved photoemission spectroscopy (ARPES). ARPES showed clear band dispersion on the surface of single-crystalline epitaxial films. The experimentally obtained band structures were compared with band-structure calculation results based on density functional theory (DFT) with generalized gradient approximation $+ U$ correction. The obtained band structures are in good agreement with the DFT calculations at $U = 2.2$ eV, suggesting that electron-electron correlation plays an important role in the electronic structure of Ti$_2$O$_3$. Furthermore, the detailed analyses with varying U suggest that the origin of the characteristic MIT in Ti$_2$O$_3$ is a semimetal-semimetal or semimetal-semiconductor transition caused by changes in the Fermi surface due to lattice deformation.

I. INTRODUCTION

Ti$_2$O$_3$, which has a corundum-type crystal structure, exhibits a unique metal-insulator transition (MIT). The bulk Ti$_2$O$_3$ is a nonmagnetic insulator with a small bandgap energy of ∼100 meV [1] at low temperatures, and it shows a transition to semimetallic states at temperatures of ∼450 K [2–9], which extends over a broad temperature of ∼150 K. This is a unique type of transition that is not observed in most other transition-metal oxide systems. Although the crystal symmetry remains unchanged across the MIT, the unit cell c/a ratio changes significantly, which suggests a close relationship between the MIT and lattice deformations [2–6,9–12].

Over the past few decades, the MIT mechanism has been experimentally and theoretically investigated [1–31]. The most relevant phenomenon in this mechanism is the overlap of the a_{1g} and e_g^π bands due to the Ti-Ti distance modulations along the c axis of the crystal lattice [5,6]. Owing to the trigonal distortions, the t_{2g} levels in TiO$_6$ octahedra further split into a lower nondegenerate a_{1g} level and higher double-degenerate e_g^π levels. The a_{1g} orbitals between the face-shared TiO$_6$ octahedra along the c axis are strongly hybridized to form a_{1g} and a_{1g}^* bands with e_g^π bands between them. When the Ti-Ti bond distances along the c axis are short, the energy splitting between the a_{1g} and a_{1g}^* bands becomes large, and consequently, the e_g^π bands do not overlap with the a_{1g} bands.

Furthermore, only the a_{1g} band is filled with Ti 3d electrons; therefore, Ti$_2$O$_3$ acts as an insulator.

The Ti$_2$O$_3$ energy diagram describes its electronic structures and reveals the close connection between the MIT and c/a ratio. In fact, the a- and c-axis lattice constants of bulk Ti$_2$O$_3$ vary significantly with temperature, and the c/a ratio increases from 2.648 to 2.701 in the range of 373–553 K across the MIT [3]. The modulation of Ti 3d electron occupations in the a_{1g} orbitals associated with a change in the c/a ratio was revealed from the temperature dependence of linear dichroism in Ti 2p x-ray absorption spectra [8,14,15].

However, the band-structure calculations challenge the validity of this simple phenomenological model because the a_{1g} and e_g^π bands always overlap for typical Ti-Ti distances [10]; a short Ti-Ti distance of < 2.2 Å is required to form the aforementioned insulating band diagram, which suggests the importance of electron-electron correlations in Ti$_2$O$_3$. To better understand the unusual physical properties of Ti$_2$O$_3$, it is necessary to collect detailed information about the complicated electronic band structure of the material.

Angle-resolved photoemission spectroscopy (ARPES) is a unique and powerful experimental technique for determining the band structure of a solid and has long played a central role in studies of the electronic properties of strongly correlated electron systems [32–48]. However, there have been few ARPES studies on Ti$_2$O$_3$ with three-dimensional corundum-type crystal structures [19]. This is mainly due to the difficulty in obtaining single-crystal surfaces of Ti$_2$O$_3$ using standard surface-preparation techniques, such as cleaving or sputtering and annealing. In addition, the chemically active surface of

*kohei.yoshimatsu.c6@tohoku.ac.jp

Ti_2O_3 [23] restricts surface-sensitive ARPES measurements on chemically well-defined surfaces. Thus, the lack of information about the band structures near the Fermi level (E_F), especially the Fermi surface (FS), has limited the understanding of the physics of Ti_2O_3.

In this paper, to elucidate the electronic structure near E_F of Ti_2O_3, we performed soft-x-ray (SX) ARPES [41–48] on single-crystalline epitaxial Ti_2O_3 films grown on α-Al_2O_3 substrates. We synthesized the films with slight hole doping by laser molecular beam epitaxy (MBE) to obtain an atomically flat and well-ordered surface. By using the well-defined surface of the epitaxial films, we clearly observed the electronic band structure of Ti_2O_3. The Ti $3d$-derived hole band forms an open triangular-pyramidal-vase-shaped FS along the Γ-A line in the hexagonal Brillouin zone (BZ). The experimental band structures were compared with the band-structure calculations based on density functional theory (DFT) with generalized gradient approximation (GGA) + U correction. Detailed analysis with varying U revealed that the obtained band structures are well described by the DFT calculations at $U = 2.2$ eV, indicating that the electron-electron correlation plays an important role in the electronic structure of Ti_2O_3. Furthermore, the comparison between the ARPES results and DFT + U calculations with varying U and c/a ratio suggests important implications regarding the origin of the characteristic MIT in Ti_2O_3; the MIT is a semimetal-semimetal or semimetal-semiconductor transition caused by changes in the FS due to lattice deformation.

II. EXPERIMENTAL

Epitaxial Ti_2O_3 films with a thickness of $\sim$100 nm were grown on α-Al_2O_3 (0001) substrates by laser MBE. A sintered TiO_x pellet was used as the ablation target [49]. A Nd:$Y_3Al_5O_{12}$ (Nd:YAG) laser was used for the target ablation using its third harmonic wave ($\lambda = 355$ nm) with a fluence of $\sim$1.5 J/cm^2 and repetition rate of 5 Hz. Before film growth, α-Al_2O_3 substrates were annealed in air at 1100 °C for 2 h to obtain an atomically flat surface with step-and-terrace structures. During the deposition, the substrate temperature was maintained at 1000 °C, and the oxygen pressure was maintained at 5×10^{-7} Torr. After deposition, the oxygen gas supply was immediately turned off, and the films were quenched to room temperature to prevent overoxidation [16,17,50,51].

After growth, the films were transferred *in vacuo* to the photoemission chamber using a mobile vacuum-transfer vessel to reduce surface contamination and additional oxidation. During transportation, the samples were under an ultra-high vacuum $<5.0 \times 10^{-10}$ Torr. Photoemission spectroscopy (PES) and ARPES were conducted at the BL-2A MUSASHI beamline of the Photon Factory, KEK. The PES spectra were recorded at 100 K using a VG-Scienta SES-2002 analyzer with total energy resolutions of 250 and 500 meV at photon energies ($h\nu$) of 800 and 1486 eV, respectively. In the ARPES experiments in the SX region of $h\nu = 300$–640 eV, the energy and angular resolutions were set to $\sim$150–250 meV and 0.25°, respectively. The ARPES experiments were also conducted at 100 K in the p-polarization geometry [35–39]. Here, E_F was inferred from gold foil in electrical connection
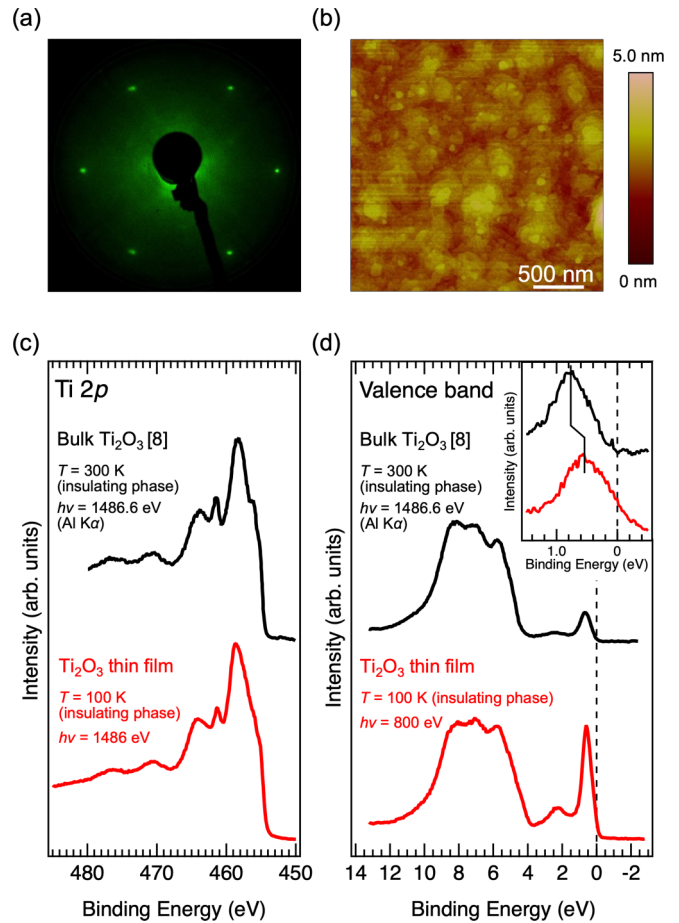

FIG. 1. (a) Low-energy electron diffraction (LEED) pattern and (b) atomic force microscopy (AFM) image of the Ti_2O_3 films grown on α-Al_2O_3 (0001) substrates. The hexagonal spots of the LEED pattern correspond to the surface Brillouin zone (BZ) projected along the [111] direction of rhombohedral Ti_2O_3. The root mean square of surface roughness of the films was estimated to be <1.0 nm in the AFM image with a $10 \times 10 \, \mu m^2$ area, demonstrating the flat surface necessary for the present spectroscopic studies. (c) Ti $2p$ core-level photoemission spectroscopy (PES) spectrum of the Ti_2O_3 films taken at 100 K (insulating phase) with a photon energy of $h\nu = 1486$ eV. (d) Corresponding valence-band spectrum taken at 800 eV. For comparison, the PES spectra of the cleaved surface of a Ti_2O_3 single crystal (black line) in an insulating phase are also shown for (c) and (d) [8]. The inset of (d) shows the comparison of the Ti $3d$-derived coherent peaks near E_F. A clear peak shift of $\sim$200 meV is observed, reflecting the hole-doped nature of the films, whereas the shape itself remains unchanged.

with the sample. The surface structure and cleanliness of the vacuum-transferred films were examined by low-energy electron diffraction (LEED) and core-level photoemission measurements immediately before the ARPES measurements. The LEED pattern of the films showed six sharp diffraction spots on a low background, as shown in Fig. 1(a), reflecting the long-range crystallinity and cleanliness of the surface. No detectable C $1s$ peak was observed in the core-level photoemission spectra (not shown). These results indicate that the Ti_2O_3 films have high surface crystallinity and cleanliness required for ARPES measurements.

The surface morphology of the measured Ti$_2$O$_3$ films was analyzed by *ex situ* atomic force microscopy (AFM) in air, and atomically flat surfaces were observed, as shown in Fig. 1(b). The crystal structure was characterized by x-ray diffraction (XRD) (see Fig. S1 in the Supplemental Material [49]), which confirmed the epitaxial growth of single-phase Ti$_2$O$_3$ films on the substrates. The out-of-plane and in-plane epitaxial relationships were Ti$_2$O$_3$ [0001] // α-Al$_2$O$_3$ [0001] and Ti$_2$O$_3$ [11–20] // α-Al$_2$O$_3$ [11–20], respectively. The temperature dependence of the electrical resistivity was measured using the standard four-probe method. The transport properties were in good agreement with previously reported values [16] (see Fig. S2 in the Supplemental Material [49]). Detailed characterizations of the grown films are presented in the Supplemental Material [49].

DFT-based band-structure calculations were conducted using QUANTUM ESPRESSO software [52,53]. The Perdew-Burke-Ernzerhof GGA was adopted as the exchange-correlation functional [54]. The kinetic energy (charge density) cutoff was set to 60 (600) Ry. The Ti and O atomic positions were optimized by the Monkhorst-Pack scheme using a $6 \times 6 \times 6$ **k**-point grid in a self-consistent scheme [55]. In the self-consistent calculation, the lattice parameters were fixed as the experimental values for the present film ($a = 5.102$ Å, $c = 13.80$ Å, and $c/a = 2.70$), which were determined by reciprocal space mapping taken at room temperature, as shown in Fig. S1(b) in the Supplemental Material [49]. The calculated FSs were visualized using FERMISURFER software [49,56]. Further computing details are described in the Supplemental Material [49].

III. RESULTS AND DISCUSSION

Before discussing the ARPES results, we provide evidence for the fact that the properties of Ti$_2$O$_3$ are retained in the surface region of the films accessible for SX-ARPES [41–48] because the surface of Ti$_2$O$_3$ is known to be extremely sensitive to oxygen and to lose the characteristic Ti^{3+}-Ti^{3+} dimer structures due to oxidation [23]. Figure 1(c) shows the Ti $2p$ core-level spectrum of the Ti$_2$O$_3$ films obtained at 100 K (insulating phase). Note that the existence of Ti^{4+} states at 459 eV due to surface overoxidation [23] is hardly seen in the spectrum. The Ti $2p$ core level exhibits the complicated multiplet structure characteristic of Ti$_2$O$_3$ single crystals [8,23]. The close similarities in the core-level spectra between the film surface and cleaved surface of Ti$_2$O$_3$ single crystals [8,23] support the fact that the chemical states in the films are almost the same as those in bulk. From the cluster-model calculation, the satellite structures were attributed to the strong bonding of the a_{1g} orbitals at the Ti-Ti dimer in Ti$_2$O$_9$ clusters [8]. Therefore, the existence of the multiplet structures demonstrates the formation of Ti^{3+}-Ti^{3+} dimers even in the surface region of the Ti$_2$O$_3$ films.

The Ti^{3+} ($3d^1$) states in the Ti$_2$O$_3$ films are also confirmed by the valence-band spectrum [Fig. 1(d)]. The spectrum mainly consists of two features: a structure derived from O $2p$ states at binding energies of 4–10 eV and a two-peak structure derived from the Ti $3d$ states near E_F [8,20–23]. The Ti $3d$ states consist of a sharp coherent peak in the vicinity of E_F and a weak broad satellite structure centered around 2.3 eV,

demonstrating the Ti^{3+} ($3d^1$) feature of Ti$_2$O$_3$. The valence bands initially seem to be almost the same between the films and bulk, which is consistent with the results of the Ti $2p$ core-level spectra, indicating that the properties of Ti$_2$O$_3$ are retained in the surface region of the films. However, a closer inspection of E_F [inset of Fig. 1(d)] reveals that there is a small but distinct density of states at E_F in the films. Furthermore, the coherent peak of the films is shifted toward the lower-binding-energy side from that of the bulk, reflecting the higher conductivity in the films (see Fig. S2 in the Supplemental Material [49]). Based on the shift of the peak positions, the chemical-potential shift due to excess hole carriers is evaluated to be ~200 meV in the Ti$_2$O$_3$ films. We will discuss the value of the chemical-potential shift in connection with the ARPES results.

From the above characterizations, we have confirmed that the Ti$_2$O$_3$ films have a long-range ordered crystalline surface without the detectable overoxidation (Ti^{4+} states) required for ARPES measurements and that characteristic Ti^{3+}-Ti^{3+} dimers are formed in the surface region of the film accessible for SX-ARPES. Thus, we address the band structure of the Ti$_2$O$_3$ films by ARPES. Figure 2(a) shows the schematic crystal structure of Ti$_2$O$_3$ in both the primitive rhombohedral unit cell and associated conventional hexagonal cell. The corresponding rhombohedral BZ is depicted in Fig. 2(b), together with an equivalent hexagonally shaped one [10]. For notational simplicity, we refer to the high-symmetry points and lines in the hexagonal BZ hereafter.

Figure 2(c) shows the out-of-plane FS map for the Ti$_2$O$_3$ films obtained from normal-emission ARPES measurements for the Γ-A-H-K emission plane [the blue hatched area in the BZ shown in Fig. 2(b)]. Reflecting the hole-doped nature, a meandering FS that follows the periodicity of the bulk BZ is clearly observed along the BZ center line (see also Fig. S12 in the Supplemental Material [49]). The cross-section of the FS is largest at the A point, monotonically decreases away from the A point, and is smallest at the Γ point. The observed FS topology was well reproduced by the DFT + U calculation with reasonable parameters (Figs. S8 and S9 in the Supplemental Material [49]), which is discussed later. The in-plane FSs at the A-H-L emission plane (taken at 500 eV) and Γ-K-M emission plane (taken at 565 eV) are shown in Figs. 2(d). A triangularlike FS is clearly observed at the A point. The overall threefold intensity pattern of the observed FS is responsible for the trigonal symmetry of Ti$_2$O$_3$, suggesting the bulk origin of the FS. Indeed, the triangularlike shape of the FS was reversed at the other A point of one point below [40] (see Fig. S14 in the Supplemental Material [49]). At the Γ point, the FS with a round shape is also observed. These results indicate the existence of an open FS in the Ti$_2$O$_3$ films. It should be noted that we did not observe any indication of other FSs outside the open FS in these measurement planes. Meanwhile, the existence of another small closed hole FS around the A point is predicted from band-structure calculations [10,49]. However, it is difficult to examine the existence of another FS inside the open FS owing to the overlap of open FS having predominant intensity (see Fig. S9 in the Supplemental Material [49]), although the existence of the other FS is suggested by normal-emission ARPES along the Γ-A
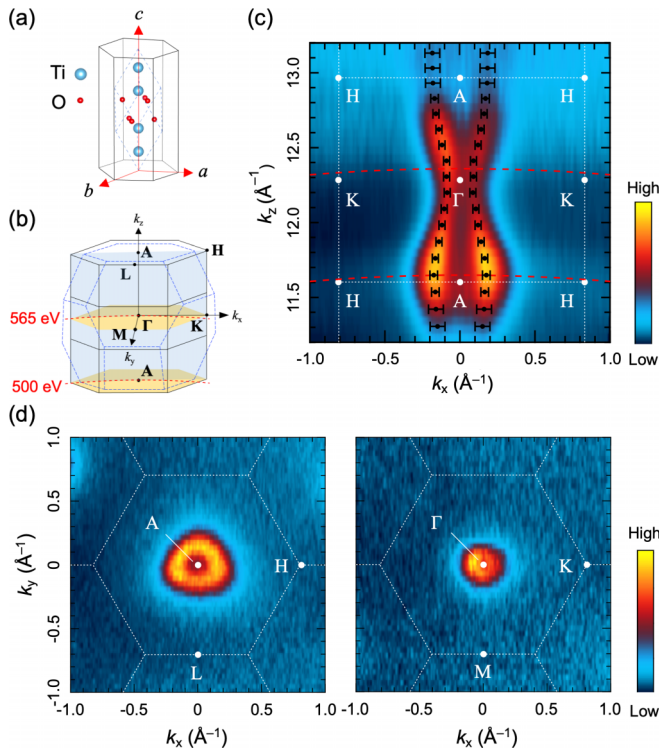
FIG. 2. (a) Crystal structure of Ti_2O_3 in primitive rhombohedral unit cell (blue dashed lines), surrounded by the conventional nonprimitive hexagonal unit cell (black solid lines). The primitive rhombohedral unit cell contains 2 f.u., while the conventional hexagonal unit cell contains 18 f.u. The red hexagonal unit vectors were determined to be $a = 5.102$ Å and $c = 13.80$ Å by x-ray diffraction (XRD) measurements (see Fig. S1 in the Supplemental Material [49]). (b) Corresponding rhombohedral Brillouin zone (BZ) and an equivalent hexagonally shaped one. In the hexagonal BZ, the high-symmetry points are labeled. The red dotted arc lines represent the **k** paths passing through the A point (at a photon energy of 500 eV) and the Γ point (at a photon energy of 565 eV). A light-blue plate represents the Γ-A-H-K emission plane where the out-of-plane Fermi surface (FS) map was measured, while two light-yellow plates represent the A-H-L and Γ-K-M emission planes for the in-plane FS mappings at corresponding energies. (c) Out-of-plane FS map in the Γ-A-H-K emission plane obtained by varying the excitation photon energies from 470 to 640 eV. The Fermi-momentum (k_F) points determined by the angle-resolved photoemission spectroscopy (ARPES) spectra are indicated by data markers. (d) In-plane FS maps acquired at the constant photon energies of 500 eV (left panel: the A-H-L emission plane) and 565 eV (right panel: the Γ-K-M emission plane) by changing emission angles. The corresponding hexagonal BZ boundaries are overlaid as white lines. The FS maps were obtained by plotting the ARPES intensity within the energy window of $E_F \pm 50$ meV.

direction (see Fig. S12 in the Supplemental Material [49]). Assuming a triangular-pyramidal shape of the open FS, the carrier density of the Ti_2O_3 films would be $\sim 2.4 \times 10^{20}$ cm^{-3}, which is consistent with the carrier density estimated from Hall effect measurements (1.1×10^{20} cm^{-3}) [16].

According to the band-structure calculation [10,49], the electronic band structure near E_F of Ti_2O_3 mainly consists of the e_g^π- and a_{1g}-derived bands. The former forms flat
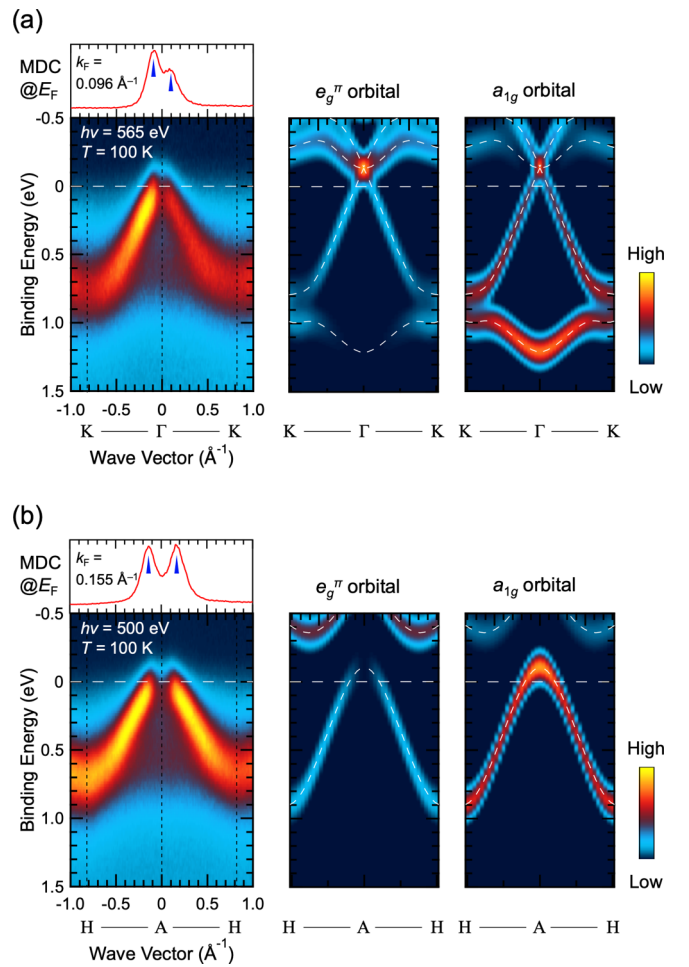

FIG. 3. Experimental band structure of the Ti_2O_3 films obtained by angle-resolved photoemission spectroscopy (ARPES) measurements (left panels) along the (a) Γ-K and (b) A-H high-symmetry lines, together with e_g^π (middle panels) and a_{1g} (right panels) orbital projected band structures. The corresponding **k** paths are illustrated in Fig. 2(c). Note that the experimental band structure is slightly asymmetric at the zone boundary, reflecting the rhombohedral Brillouin zone (BZ). The momentum distribution curves (MDCs) at E_F with an energy window of ± 5 meV are shown in the upper panel for each experimental band structure. The blue triangles indicate the Fermi momentum (k_F). In the orbital projections, the band structure is overlaid by white dotted lines.

(dispersive) bands, while the latter forms dispersive (flat) bands along the out-of-plane (in-plane) direction, reflecting their anisotropic orbital shape. The e_g^π-derived band forms an electron pocket(s) at the Γ point, whereas the a_{1g}-derived band forms a hole pocket(s) at the A point. The slight overlap between the two pockets makes intrinsic Ti_2O_3 a compensated semimetal. This semimetallic nature may be the origin of the unusual physical properties of Ti_2O_3 because the delicate balance between the energy of the e_g^π and a_{1g} states causes a notable change in the conduction-carrier character as a result of hybridization with the other states. Thus, it is worth investigating the band structure near E_F. Figure 3 shows the experimental band structures along the in-plane high-symmetry directions [the Γ-K and A-H lines in Figs. 3(a)

and 3(b), respectively]. The corresponding energy distribution curves (EDCs) along each line are shown in Fig. S15 in the Supplemental Material [49]. As expected from the FS maps in Fig. 2, highly dispersive hole bands exist at both Γ and A points and form an FS at the zone center, reflecting the existence of hole carriers. The bands cross E_F at Fermi momentum $k_F = 0.096\,\text{Å}^{-1}$ ($0.155\,\text{Å}^{-1}$) around the Γ (A) point, while they disperse down to ~700 meV around the zone boundary.

To investigate the band structure near E_F in more detail, we compared the experimental band structure with the DFT calculation based on the GGA $+ U$ approximation using the reasonable parameters consistent with the experimental facts [17,49]. According to the DFT $+ U$ calculation, the band structures, especially the FS topology, of Ti$_2$O$_3$ strongly depend on the parameters of U and c/a ratio (Figs. S5–S7 in the Supplemental Material [49]). Herein, we used $U = 2.2$ eV to reproduce the insulating phase of bulk Ti$_2$O$_3$, which exhibits an energy gap of ~100 meV at a c/a ratio of 2.639 [17]. Moreover, the c/a ratio, which also governs the electronic properties of Ti$_2$O$_3$, was fixed at 2.70 as determined from the XRD measurements (see Fig. S1 in the Supplemental Material [49]). The results of the DFT calculations are shown in the panels of Fig. 3, where the Fermi level in the DFT calculations is shifted by 180 meV toward the higher-binding-energy side to reproduce the k_F value of the hole pocket at the Γ point. This is because the electron pocket is always formed at the Γ point in DFT calculations irrespective of U values and c/a ratios for Ti$_2$O$_3$ with metallic ground states (see Figs. S5–S7 in the Supplemental Material [49]). It should be noted that the shift of the Fermi level is consistent with the chemical-potential shift estimated from the shift of the Ti $3d$ coherent peak, as seen in the inset of Fig. 1(d).

The ARPES results and DFT calculations show fairly good agreement. According to the orbital projected band structures shown in Fig. 3 (also see Fig. S4 in the Supplemental Material [49]), the hole band centered at the Γ point is assigned to the e_g^π-derived band. The hole band has a substantial e_g^π character at the Γ point, while it loses the e_g^π character rapidly apart from the zone center owing to strong hybridization with other states. Meanwhile, the other hole FSs centered at the A point fundamentally consist of two a_{1g}-derived hole bands, which degenerate along the A-H line. The a_{1g}-derived hole bands have an a_{1g} character at the A point, while they are strongly hybridized with the e_g^π and e_g^σ states apart from the zone center. As can be seen in Fig. 3, the present ARPES results predominantly show the band to have significant e_g^π-orbital weight owing to the dipole selection rules for p polarization of the incident light and measurement geometry used [32,33,57].

Next, to demonstrate the importance of electron-electron correlation, we compare the band dispersion determined by ARPES with the DFT calculation in more detail. Figure 4 shows the band dispersion drawn based on the ARPES peak positions determined from the EDCs and MDCs, together with the DFT $+ U$ calculations. The band-structure calculation was also conducted at $U = 0$ eV as a reference for clarifying the effect of the electron-electron correlation. Note that the band dispersion of $U = 0$ eV is almost identical to that previously reported [10]. As can be seen in Fig. 4, the overall band structure is in good agreement with the DFT calculation at $U = 2.2$ eV; the dispersion of the e_g^π-derived hole band
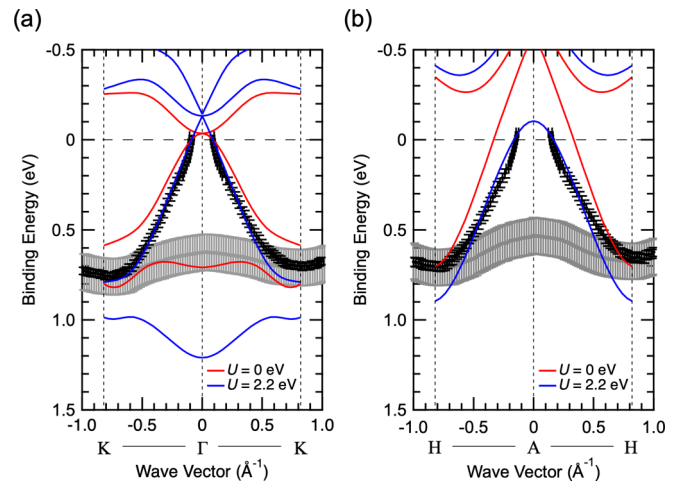

FIG. 4. Comparison of the experimental band structure with generalized gradient approximation (GGA) $+ U$ calculation. Peak positions determined from energy distribution curves (EDCs) and momentum distribution curves (MDCs) are plotted by the data markers. The black and gray markers indicate the peak positions of the dispersive and nondispersive quasilocalized states, respectively. The results of GGA $+ U$ calculation with $U = 0$ and 2.2 eV are plotted as the red and blue lines, respectively. The Fermi level of the band structure calculations with $U = 2.2$ eV (0 eV) was shifted by 180 meV (150 meV) toward the higher-binding-energy side to reproduce the experimental k_F value at the Γ point. The sudden upturn of band dispersion starting from E_F may originate from the interplay of the energy resolution and Fermi-edge cutoff [58].

centered at the Γ point is quite well reproduced. In addition, k_F along the A-H direction shows excellent agreement between the experiment and calculation, indicating the validity of $U = 2.2$ eV and the Fermi level correction for describing the electronic structures of the hole-doped Ti$_2$O$_3$ films.

Meanwhile, in the calculation, a flat band exists at a higher binding energy along the Γ-K direction. The flat band originates from the a_{1g} orbital and forms a hole pocket at the A point, reflecting the anisotropic feature of the a_{1g} orbital with a large distribution along the [0001] direction (Fig. S4 in the Supplemental Material [49]). The band is barely seen in the ARPES images in Fig. 3(a), although the existence of the a_{1g}-derived band itself is confirmed by normal emission ARPES along the Γ-A direction (see Figs. S12 and S13 in the Supplemental Material [49]). The very weak intensity is probably caused by the dipole selection rules for the a_{1g} orbital in the present experimental geometry [35–39], as demonstrated in Fig. 3(a). Furthermore, the presence of a broad nondispersive component at 0.5–0.6 eV masks the details of the band dispersion along the Γ-K direction. Therefore, it is difficult to determine the energy position of the band at the Γ point from the present data. The nondispersive states can also be seen in the ARPES image along the A-H direction [Fig. 3(b)], where such a flat band is not predicted by the DFT calculation [Fig. 4(b)]. It should be noted that, in contrast to the case of CrO$_2$ [42], such nondispersive states cannot be found in the DFT calculation even with increasing U (see Fig. S5 in the Supplemental Material [49]) for the case of Ti$_2$O$_3$. Although the origin of the nondispersive states is currently

not clear, similar nondispersive quasilocalized states other than the lower Hubbard band (incoherent part) have also been observed in V_2O_3 [41], implying that these nondispersive states are a common feature at the surface of corundum-type conductive oxides.

In contrast to $U = 2.2\,\mathrm{eV}$, there is less agreement between the experiment and calculation at $U = 0\,\mathrm{eV}$. A significant discrepancy is observed in the a_{1g}-derived bands along the *A-H* direction [Fig. 4(b)]. Note that we attempted to adjust the Fermi level for $U = 0\,\mathrm{eV}$ to improve this discrepancy, but we did not find any improvement in the k_F positions along with both the Γ-*K* and *A-H* directions. These results suggest the importance of the electron-electron correlation for describing the electronic structure of Ti_2O_3.

The disagreement between the experiment and calculation at $U = 0\,\mathrm{eV}$ likely originates from the difference in the energy levels of the a_{1g} and e_g^{π} states. For the band dispersions in the DFT + U calculations with varying U (see Figs. S5 and S6 in the Supplemental Material [49]), the energy separation between the a_{1g} and e_g^{π} states increases with increasing U; the a_{1g}-derived band is pushed down, whereas the e_g^{π}-derived band is pushed up. The increment of U causes narrowing of the a_{1g}-derived band dispersion along the *A-H* direction and widening of the e_g^{π}-derived band dispersion along the Γ-*K* direction. As a result, the electron and hole pockets at the Γ and *A* points, respectively, simultaneously become smaller, and eventually a tiny energy gap opens at $U = 2.5\,\mathrm{eV}$. Accordingly, the occupancy of the lowest-lying a_{1g} state increases with increasing U.

The semimetallic ground states of Ti_2O_3 predominantly originate from the slight overlap between the e_g^{π}-derived electron pocket at the Γ point and the a_{1g}-derived hole pockets at the *A* point (at the midpoint of the Γ-*A* line for $U = 2.2\,\mathrm{eV}$; see Fig. S5 in the Supplemental Material [49]). The increment of U reduces the degree of the overlap. Therefore, the excellent agreements in k_F between the ARPES and DFT calculations at $U = 2.2\,\mathrm{eV}$ indicate that the electron-electron correlation plays an essential role in the band structures of Ti_2O_3. The sensitivity of k_F (FS topology) to U triggers an additional check for the validity of $U = 2.2\,\mathrm{eV}$ to describe the electronic band structure of the Ti_2O_3 films. Difference in k_F at the *A* point between the ARPES and DFT calculations with varying U (Figs. S10 and S11 in the Supplemental Material [49]) suggests that the best match is obtained at $U = 2.2\,\mathrm{eV}$. This indicates the validity of the U value of 2.2 eV.

The importance of electron-electron correlation is further supported by the ARPES results shown in Fig. 4, where an almost identical bandwidth between the experiment and calculation is observed along both the Γ-*K* and *A-H* lines. Meanwhile, reduction of the overlapping was also achieved by shortening the Ti-Ti bond distances along the *c* axis (or equivalently, by reducing the *c/a* ratio; see Fig. S7 in the Supplemental Material [49]), although an unusually short Ti-Ti distance of $<2.2\,\text{Å}$ was required to form the insulating ground state in Ti_2O_3 without U [10]. Thus, it should be considered that the FS topology of Ti_2O_3 is governed by a delicate balance between the electron-electron correlations and lattice deformations and, consequently, is very sensitive to both. Additionally, bear in mind that, in this paper, we have not ruled out the possible contribution of dynamic electronic correlations to the MIT, namely, the possibility of Ti-Ti dimer deformation-assisted Mott transition in Ti_2O_3 [25]. Thus, a more elaborate band-structure calculation that adjusts both the effects and incorporates the dynamic electronic correlations in a realistic manner is necessary to reproduce the ARPES results as well as the physical properties of Ti_2O_3 [11,24,25].

Finally, we discuss the possible origin of the MIT in Ti_2O_3. From the band structure shown in Fig. 4 (also see Fig. S3 in the Supplemental Material [49]), intrinsic Ti_2O_3 exhibits a semimetallic band structure, where the electron pocket at the Γ point and hole pocket at the midpoint of the Γ-*A* line for $U = 2.2\,\mathrm{eV}$ (at the *A* point for $U = 0\,\mathrm{eV}$) slightly overlap in energy. In general, for such a small carrier system, the influence of the electron-electron correlation on phase-transition phenomena is not significantly large [31], whereas a slight change in a band structure significantly changes the FS topology and resultant transport properties. Meanwhile, it is known that lattice deformation occurs in Ti_2O_3 regardless of the doping concentration [3,7,30]. Therefore, the most plausible scenario is that the MIT of Ti_2O_3 is a semimetal-semimetal or semimetal-semiconductor transition caused by the changes in the FS topology due to lattice deformation, not a filling-controlled MIT [31]. In fact, the MIT temperature of $(Ti_{1-x}V_x)_2O_3$ remains almost unchanged with x, even though the carrier density changes notably; consequently, the ground state changes from insulator at $x = 0$ to metal at $x = 0.06$ [7]. To verify the possibility of semimetal-semimetal or semimetal-semiconductor transition in Ti_2O_3 caused by the changes in the FS topology due to lattice deformation, further investigations are required; detailed temperature-dependent studies on both the crystal and electronic structures are necessary.

IV. CONCLUSIONS

To investigate the electronic band structure near E_F of Ti_2O_3, we performed SX-ARPES on single-crystalline epitaxial Ti_2O_3 films grown on α-Al_2O_3 substrates. Using well-defined surfaces of the epitaxial films, we clearly observed the electronic band structure of Ti_2O_3. The Ti 3*d*-derived band forms an open hole FS with a triangular-pyramidal vase shape along the Γ-*A* line in the hexagonal BZ, which is in line with the previous transport measurements. We also found the highly dispersive e_g^{π}- and a_{1g}-derived bands centered at the Γ and *A* points, respectively. The observed band structures were compared with the band-structure calculations based on DFT with GGA + U correction. Detailed analysis with varying U revealed that the obtained band structure is well described by the DFT calculation at $U = 2.2\,\mathrm{eV}$. These results suggest that the electron-electron correlation plays an important role in describing the overall electronic structure of Ti_2O_3. Nevertheless, the influence of electron-electron correlation on the quantum phase transition in Ti_2O_3 is considered weak owing to its low carrier density. Therefore, the ARPES and DFT calculation results presented here have important implications regarding the origin of the characteristic MIT in Ti_2O_3; the MIT is a semimetal-semimetal or semimetal-semiconductor transition caused by changes in the FS topology due to lattice deformation.

[1] J. M. Honig and T. B. Reed, Electrical properties of Ti$_2$O$_3$ single crystals, Phys. Rev. **174**, 1020 (1968).

[2] J. M. Honig, Nature of the electrical transition in Ti$_2$O$_3$, Rev. Mod. Phys. **40**, 748 (1968).

[3] J. J. Capponi, M. Marezio, J. Dumas, and C. Schlenker, Lattice parameters variation with temperature of Ti$_2$O$_3$ and (Ti$_{0.98}$V$_{0.02}$)$_2$O$_3$ from single crystal x-ray data, Solid State Commun. **20**, 893 (1976).

[4] C. N. R. Rao, R. E. Loehman, and J. M. Honig, Crystallographic study of the transition in Ti$_2$O$_3$, Phys. Lett. A **27**, 271 (1968).

[5] L. L. Van Zandt, J. M. Honig, and J. B. Goodenough, Resistivity and magnetic order in Ti$_2$O$_3$, J. Appl. Phys. **39**, 594 (1968).

[6] H. J. Zeiger, Unified model of the insulator-metal transition in Ti$_2$O$_3$ and the high-temperature transitions in V$_2$O$_3$, Phys. Rev. B **11**, 5132 (1975).

[7] M. Uchida, J. Fujioka, Y. Onose, and Y. Tokura, Charge Dynamics in Thermally and Doping Induced Insulator-Metal Transitions of (Ti$_{1-x}$V$_x$)$_2$O$_3$, Phys. Rev. Lett. **101**, 066406 (2008).

[8] C. F. Chang, T. C. Koethe, Z. Hu, J. Weinen, S. Agrestini, L. Zhao, J. Gegner, H. Ott, G. Panaccione, H. Wu *et al.*, *C*-Axis Dimer and Its Electronic Breakup: The Insulator-to-Metal Transition in Ti$_2$O$_3$, Phys. Rev. X **8**, 021004 (2018).

[9] G. V. Chandrashekhar, Q. Won Choi, J. Moyo, and J. M. Honig, The electrical transition in V-doped Ti$_2$O$_3$, Mater. Res. Bull. **5**, 999(1970).

[10] L. F. Mattheiss, Electronic structure of rhombohedral Ti$_2$O$_3$, J. Phys.: Condens. Mater. **8**, 5987 (1996).

[11] V. Singh and J. J. Pulikkotil, Electronic phase transition and transport properties of Ti$_2$O$_3$, J. Alloys Compd. **658**, 430 (2016).

[12] Y. Tsujimoto, Y. Matsushita, S. Yu, K. Yamaura, and T. Uchikoshi, Size dependence of structural, magnetic, and electrical properties in corundum-type Ti$_2$O$_3$ nanoparticles showing insulator-metal transition, J. Asian Ceram. Soc. **3**, 325 (2015).

[13] F. J. Morin, Oxides Which Show a Metal-To-Insulator Transition at the Neel Temperature, Phys. Rev. Lett. **3**, 34 (1959).

[14] A. Tanaka, On the metal-insulator transitions in VO$_2$ and Ti$_2$O$_3$ from a unified viewpoint, J. Phys. Soc. Jpn. **73**, 152 (2004).

[15] H. Sato, A. Tanaka, M. Sawada, F. Iga, K. Tsuji, M. Tsubota, M. Takemura, K. Yaji, M. Nagira, A. Kimura *et al.*, Ti 3*d* orbital change across metal-insulator transition in Ti$_2$O$_3$: polarization-dependent soft x-ray absorption spectroscopy at Ti 2*p* edge, J. Phys. Soc. Jpn. **75**, 053702 (2006).

[16] K. Yoshimatsu, H. Kurokawa, K. Horiba, H. Kumigashira, and A. Ohtomo, Large anisotropy in conductivity of Ti$_2$O$_3$ films, APL Mater. **6**, 101101 (2018).

[17] K. Yoshimatsu, N. Hasegawa, Y. Nambu, Y. Ishii, Y. Wakabayashi, and H. Kumigashira, Metallic ground states of undoped Ti$_2$O$_3$ films induced by elongated *c*-axis lattice constant, Sci. Rep. **10**, 22109 (2020).

[18] Y. Guo, S. J. Clark, and J. Robertson, Electronic and magnetic properties of Ti$_2$O$_3$, Cr$_2$O$_3$, and Fe$_2$O$_3$ calculated by the screened exchange hybrid density functional, J. Phys.: Condens. Mater. **24**, 325504 (2012).

[19] K. E. Smith and V. E. Henrich, Bulk band dispersion in Ti$_2$O$_3$ and V$_2$O$_3$, Phys. Rev. B **38**, 5965 (1988).

[20] T. Uozumi, K. Okada, A. Kotani, Y. Tezuka, and S. Shin, Ti 2*p* and resonant 3*d* photoemission spectra of Ti$_2$O$_3$, J. Phys. Soc. Jpn. **65**, 1150 (1996).

[21] J. M. McKay, M. H. Mohamed, and V. E. Henrich, Localized 3*p* excitations in 3*d* transition-metal-series spectroscopy, Phys. Rev. B **35**, 4304 (1987).

[22] A. Mooradian and P. M. Raccah, Raman study of the semiconductor-metal transition in Ti$_2$O$_3$, Phys. Rev. B **3**, 4253 (1971).

[23] S. A. Chambers, M. H. Engelhard, L. Wang, T. C. Droubay, M. E. Bowden, M. J. Wahila, N. F. Quackenbush, L. F. J. Piper, T.-L. Lee, C. J. Nelin *et al.*, X-ray photoelectron spectra for single-crystal Ti$_2$O$_3$: experiment and theory, Phys. Rev. B **96**, 205143 (2017).

[24] F. Iori, M. Gatti, and A. Rubio, Role of nonlocal exchange in the electronic structure of correlated oxides, Phys. Rev. B **85**, 115129 (2012).

[25] A. I. Poteryaev, A. I. Lichtenstein, and G. Kotliar, Nonlocal Coulomb Interaction and Metal-Insulator Transition in Ti$_2$O$_3$: A Cluster LDA + DMFT Approach, Phys. Rev. Lett. **93**, 086401 (2004).

[26] H. Nakatsugawa and E. Iguchi, Transition phenomenon in Ti$_2$O$_3$ using the discrete variational *xα* cluster method and periodic shell model, Phys. Rev. B **56**, 12931 (1997).

[27] S. H. Shin, R. L. Aggarwal, B. Lax, and J. M. Honig, Raman scattering in Ti$_2$O$_3$-V$_2$O$_3$ alloys, Phys. Rev. B **9**, 583 (1974).

[28] S. H. Shin, F. H. Pollak, T. Halpern, and P. M. Raccah, Resonance Raman scattering in Ti_2O_3 in the range 1.8–2.7 eV, Solid State Commun. **16**, 687 (1975).

[29] A. Tanaka, A new scenario on the metal-insulator transition in VO_2, J. Phys. Soc. Jpn. **72**, 2433 (2003).

[30] C. E. Rice and W. R. Robinson, Structural changes in the solid solution $(Ti_{1-x}V_x)_2O_3$ as a varies from zero to one, J. Solid State Chem. **21**, 145 (1977).

[31] M. Imada, A. Fujimori, and Y. Tokura, Metal-insulator transitions, Rev. Mod. Phys. **70**, 1039 (1998).

[32] A. Damascelli, Probing the electronic structure of complex systems by ARPES, Phys. Scr. **2004**, 61 (2004).

[33] A. Damascelli, Z. Hussain, and Z.-X. Shen, Angle-resolved photoemission studies of the cuprate superconductors, Rev. Mod. Phys. **75**, 473 (2003).

[34] J. A. Sobota, Y. He, and Z.-X. Shen, Angle-resolved photoemission studies of quantum materials, Rev. Mod. Phys. **93**, 025006 (2021).

[35] M. Kobayashi, K. Yoshimatsu, E. Sakai, M. Kitamura, K. Horiba, A. Fujimori, and H. Kumigashira, Origin of the Anomalous Mass Renormalization in Metallic Quantum Well States of Strongly Correlated Oxide $SrVO_3$, Phys. Rev. Lett. **115**, 076801 (2015).

[36] M. Kobayashi, K. Yoshimatsu, T. Mitsuhashi, M. Kitamura, E. Sakai, R. Yukawa, M. Minohara, A. Fujimori, K. Horiba, and H. Kumigashira, Emergence of quantum critical behavior in metallic quantum-well states of strongly correlated oxides, Sci. Rep. **7**, 16621 (2017).

[37] T. Mitsuhashi, M. Minohara, R. Yukawa, M. Kitamura, K. Horiba, M. Kobayashi, and H. Kumigashira, Influence of $k_\perp$ broadening on ARPES spectra of the (110) and (001) surfaces of $SrVO_3$ films, Phys. Rev. B **94**, 125148 (2016).

[38] T. Kanda, D. Shiga, R. Yukawa, N. Hasegawa, D. K. Nguyen, X. Cheng, R. Tokunaga, M. Kitamura, K. Horiba, K. Yoshimatsu *et al.*, Electronic structure of $SrTi_{1-x}V_xO_3$ films studied by in situ photoemission spectroscopy: screening for a transparent electrode material, Phys. Rev. B **104**, 115121 (2021).

[39] R. Yukawa, M. Kobayashi, T. Kanda, D. Shiga, K. Yoshimatsu, S. Ishibashi, M. Minohara, M. Kitamura, K. Horiba, A. F. Santander-Syro *et al.*, Resonant tunneling driven metal-insulator transition in double quantum-well structures of strongly correlated oxide, Nat. Commun. **12**, 7070 (2021).

[40] I. Lo Vecchio, J. D. Denlinger, O. Krupin, B. J. Kim, P. A. Metcalf, S. Lupi, J. W. Allen, and A. Lanzara, Fermi Surface of Metallic V_2O_3 from Angle-Resolved Photoemission: Mid-level Filling of e_g^π Bands, Phys. Rev. Lett. **117**, 166401 (2016).

[41] M. Thees, M.-H. Lee, R. L. Bouwmeester, P. H. Rezende-Gonçalves, E. David, A. Zimmers, F. Fortuna, E. Frantzeskakis, N. M. Vargas, Y. Kalcheim *et al.*, Imaging the itinerant-to-localized transmutation of electrons across the metal-to-insulator transition in V_2O_3, Sci. Adv. **7**, eabj1164 (2021).

[42] F. Bisti, V. A. Rogalev, M. Karolak, S. Paul, A. Gupta, T. Schmitt, G. Güntherodt, V. Eyert, G. Sangiovanni, G. Profeta *et al.*, Weakly-Correlated Nature of Ferromagnetism in Nonsymmorphic CrO_2 Revealed by Bulk-Sensitive Soft-X-Ray ARPES, Phys. Rev. X **7**, 041067 (2017).

[43] V. N. Strocov, A. Chikina, M. Caputo, M.-A. Husanu, F. Bisti, D. Bracher, T. Schmitt, F. Miletto Granozio, C. A. F. Vaz, and

[44] F. Lechermann, Electronic phase separation at $LaAlO_3/SrTiO_3$ interfaces tunable by oxygen deficiency, Phys. Rev. Mater. **3**, 106001 (2019).

[45] A. Chikina, D. V. Christensen, V. Borisov, M.-A. Husanu, Y. Chen, X. Wang, T. Schmitt, M. Radovic, N. Nagaosa, A. S. Mishchenko *et al.*, Band-order anomaly at the γ-$Al_2O_3/SrTiO_3$ interface drives the electron-mobility boost, ACS Nano **15**, 4347 (2021).

[45] V. N. Strocov, L. L. Ley, M. Kobayashi, C. Cancellieri, M.-A. Husanu, A. Chikina, N. B. M. Schröter, X. Wang, J. A. Krieger, and Z. Salman, k-resolved electronic structure of buried heterostructure and impurity systems by soft-x-ray ARPES, J. Electron Spectrosc. Relat. Phenom. **236**, 1 (2019).

[46] L. L. Lev, J. Krempaský, U. Staub, V. A. Rogalev, T. Schmitt, M. Shi, P. Blaha, A. S. Mishchenko, A. A. Veligzhanin, Y. V. Zubavichus *et al.*, Fermi Surface of Three-Dimensional $La_{1-x}Sr_xMnO_3$ Explored by Soft-X-Ray ARPES: Rhombohedral Lattice Distortion and Its Effect on Magnetoresistance, Phys. Rev. Lett. **114**, 237601 (2015).

[47] M.-A. Husanu, L. Vistoli, C. Verdi, A. Sander, V. Garcia, J. Rault, F. Bisti, L. L. Lev, T. Schmitt, F. Giustino *et al.*, Electron-polaron dichotomy of charge carriers in perovskite oxides, Commun. Phys. **3**, 62 (2020).

[48] G. Berner, M. Sing, H. Fujiwara, A. Yasui, Y. Saitoh, A. Yamasaki, Y. Nishitani, A. Sekiyama, N. Pavlenko, T. Kopp *et al.*, Direct K-Sapce Mapping of the Electronic Structure in an Oxide-Oxide Interface, Phys. Rev. Lett. **110**, 247601 (2013).

[49] See Supplemental Material at http://link.aps.org/supplemental/10.1103/PhysRevB.105.235137 for preparation of TiO_x ceramic target, crystal structures of the films, transport properties of the films, band-structure calculations, and analysis details of the ARPES data.

[50] K. Yoshimatsu, O. Sakata, and A. Ohtomo, Superconductivity in Ti_4O_7 and γ-Ti_3O_5 films, Sci. Rep. **7**, 12544 (2017).

[51] H. Kurokawa, K. Yoshimatsu, O. Sakata, and A. Ohtomo, Effects of phase fraction on superconductivity of low-valence eutectic titanate films, J. Appl. Phys. **122**, 055302 (2017).

[52] P. Giannozzi, S. Baroni, N. Bonini, M. Calandra, R. Car, C. Cavazzoni, D. Ceresoli, G. L. Chiarotti, M. Cococcioni, I. Dabo *et al.*, QUANTUM ESPRESSO: a modular and open-source software project for quantum simulations of materials, J. Phys.: Condens. Matter **21**, 395502 (2009).

[53] P. Giannozzi, O. Andreussi, T. Brumme, O. Bunau, M. B. Nardelli, M. Calandra, R. Car, C. Cavazzoni, D. Ceresoli, M. Cococcioni *et al.*, Advanced capabilities for materials modelling with QUANTUM ESPRESSO, J. Phys.: Condens. Matter **29**, 465901 (2017).

[54] J. P. Perdew, K. Burke, and M. Ernzerhof, Generalized Gradient Approximation Made Simple, Phys. Rev. Lett. **77**, 3865 (1996).

[55] H. J. Monkhorst and J. D. Pack, Special points for Brillouin-zone integrations, Phys. Rev. B **13**, 5188 (1976).

[56] M. Kawamura, FermiSurfer: Fermi-surface viewer providing multiple representation schemes, Comp. Phys. Commun. **239**, 197 (2019).

[57] S. Hüfner, *Photoelectron Spectroscopy* (Springer-Verlag, Berlin, 1995).

[58] G. Levy, W. Nettke, B. M. Ludbrook, C. N. Veenstra, and A. Damascelli, Deconstruction of resolution effects in angle-resolved photoemission, Phys. Rev. B **90**, 045150 (2014).